



OPEN

High-performance optoelectronic and thermoelectric properties of transparent conductors based on Tl_2O_3 under pressure

H. A. Rahnamaye Aliabad¹✉, A. Asadpour Arzefooni¹, Seyede Zeinab Sadati¹, Evren Görkem Özdemir² & P. Khosrojerdi¹

In this work, the full-potential linearized augmented plane wave method (FP-LAPW) and the modified Becke-Johnson (mBJ) functional with spin-orbit (SO) coupling are used to obtain the structural, optoelectronic and thermoelectric properties of Tl_2O_3 under pressure. The results show that Tl_2O_3 , as transparent conducting oxide (TCO), is a direct bandgap semiconductor with a band gap of 1.23 eV. The band gap value and the effective mass of electrons increases by increasing pressure. Density of state spectra reveal that the nature of electrons in Tl-6s state in the bottom of conduction band, like free electrons in s state, is responsible for the conducting behavior of Tl_2O_3 . A blue shift is observed in optical spectra such as electron energy loss and absorption spectra with an increase in pressure. Obtained dielectric constants under pressure are inversely proportional to the band gap value according to Penn model. The effects of pressure on thermometric properties are also explored. The hydrostatic pressure increases Seebeck coefficient, while it decreases thermal conductivity that is an effective way to the enhancement of the thermoelectric efficiency of TCOs. A figure of merit (ZT) of 0.98 in p-type Tl_2O_3 is achieved that is desirable for using in thermoelectric devices.

Keywords Tl_2O_3 , Optoelectronic and thermoelectric properties, Pressure, DFT

Transparent thermoelectric materials have been extensively investigated in clean and renewable energy sources. Transparent conducting oxides (TCOs) such as Tl_2O_3 , In_2O_3 , TiO_2 , SnO_2 , and ZnO are used in liquid crystal and touch-screen displays, photovoltaic cells, and thermoelectric devices due to their transparency in the visible light range and attractive electronic properties^{1–4}. The computed hole mobility for Li_3Sb is quite exceptional and comparable with the electron mobility in the best n-type TCOs⁵.

Among the TCOs with bixbyite structure, Tl_2O_3 is a degenerate n-type semiconductor with high conductivity and very low resistivity of about $10^{-4} \Omega \text{ cm}^{-16}$. In Tl_2O_3 transparent conductor^{7–10}, the carrier concentration changes significantly with oxygen partial pressure^{10–13} and semiconducting nature is observed by defect-induced in the crystal structure of compound. The metallic behavior of Tl_2O_3 probably originates from oxygen vacancy defects⁹.

The experimental and theoretical studies show that optical band gap of Tl_2O_3 change from 1.40 to 2.75 eV^{8,11,14} and 0.33 to 0.6 eV^{7,14}, respectively. This difference in band gap values originate from additional electrons introduced into the material by some n-type defects, and self-doping due to the oxygen vacancy formation^{7,9}. The carrier concentration of Tl_2O_3 increase by defects and the oxygen vacancies and reach $7.6 \times 10^{20} \text{ cm}^{-39}$. Thallium-doping with the electron configuration of $[\text{Xe}] 6s^2 4f^{14} 5d^{10} 6p^1$ is suitable way to reduces the band gap and increase the carrier mobility of In_2O_3 ¹⁵.

In the new TCOs, such as ZnSb_2O_6 (Ga-doping)¹⁶ and Ga_2O_3 (Si-doping)¹⁷ compounds, the band gap values for the pure and doped-TCOs increases from 3.38 to 3.56 eV and 4.80 to 4.99 eV, respectively. The widening of the band gap is due to the Burstein-Moss (B. M.) shift.

The band gap value can be altered by change in the carrier concentrations from E_g to \hat{E}_g as the Burstein-Moss (B. M.) effect⁷. The B. M. shifts of the band gap is due to the filling the bottom of the conduction band. The band gap value is given by Ref.¹⁸:

¹Department of Physics, Hakim Sabzevari University, Sabzevar 96179–76487, Iran. ²Department of Physics, Faculty of Science, Gazi University, Teknikokullar, 06560 Ankara, Turkey. ✉email: Rahnama@hsu.ac.ir

$$\dot{E}_g = E_g + \Delta E_g^{BM}, \quad (1)$$

where ΔE_g^{BM} is the Burstein–Moss energy shift given by:

$$\Delta E_g^{BM} = \frac{\hbar^2}{2m_{vc}^*} (3\pi^2 n_e)^{2/3} \quad (2)$$

Optical transitions of carriers are interpreted by considering the Burstein–Moss (B. M.) shift in the conduction band¹³. Optical reflectivity spectra show that there is a strong reflectance in the near-infrared region (1300–1500 nm)¹⁴. The B. M. mechanism is observed in transparent conductors like Ti_2O_3 and narrow band gap materials for using in solar cells and high-temperature thallium oxide-based superconductors¹⁹. Narrow band gap materials are typically good thermoelectric materials²⁰. However, development of transparent conductors with high thermoelectric efficiencies is one of effective ways to produce electricity without losing their transparency. Narrow electronic states play a key role in the TCOs for thermoelectric applications.

The structural, optical, and thermoelectric properties are sensitive to the applied pressure²¹. On the other hand, the effect of pressure has been a powerful method for studying the optoelectronic and thermoelectric properties of materials in the past few decades. The thermoelectric efficiency of a material can be improved by applying pressure^{22–29}.

The efficiency of thermoelectric materials is defined by the figure of merit, $ZT = S^2\sigma T/\kappa$, where S , σ , T and κ are the Seebeck coefficient, electrical conductivity, absolute temperature, and total thermal conductivity, respectively. It is clear that high ZT value requires high σ , low κ , and relatively high S . The electronic structure of materials is important for the reach high ZT values²².

The experimental results show that Ti_2O_3 has a cubic bixbyite crystal structure with $Ia\bar{3}$ space group and lattice constant of $a = 10.5344 \text{ \AA}$ ³⁰. Gomis et al. have studied the structural properties of Ti_2O_3 under high pressures³¹. Their results indicate that the crystal structure of Ti_2O_3 is cubic bixbyite to 22.0 GPa. At room temperature, the amorphous phase of Ti_2O_3 is predicted above 22 GPa by the theoretical analysis of the elastic properties³¹.

In the present work, we have investigated the structural, optoelectronic, and thermoelectric transport properties of Ti_2O_3 under high pressures up to 22.0 GPa by using the DFT as implemented in the Wien2k³² and BoltzTrap codes³³. The method of calculations is described in Sect. "Computational details". The optoelectronic and thermoelectric results are presented and discussed in Sect. "Results and discussions" and conclusions is summarized in Sect. "Conclusion".

Computational details

Pressure-dependent optoelectronic and transport properties of Ti_2O_3 were calculated by the full-potential linearized augmented plane wave method (FP-LAPW). For calculation of the exchange–correlation potentials, the modified Becke–Johnson (mBJ) functionals^{34–38} with spin–orbit coupling are used as implemented in the Wien2k package. The electronic wave functions are expanded by the plane-wave cutoff value of $K_{\max} \times R_{\text{MT}} = 7.0$ in the interstitial region (R_{MT} is the smallest atomic muffin tin sphere radius). G_{\max} , the magnitude of the largest vector in the Fourier expansion of charge density, is selected about 12 (Ry)^{1/2}. The self-consistent field (SCF) calculations are carried out with 600, 1800, and 12,000 k-points for structural, optoelectronic, and thermoelectric calculations, respectively.

The Boltzmann transport equation by employment of the rigid band approximation is used to obtain the thermoelectric properties. In this approximation, a shift of the Fermi level is equivalent to the doping of the compound. The Fermi level is defined as: $E_f = \frac{\hbar^2}{2m^*} (3\pi^2 n)^{2/3}$, where n and m^* are carrier concentration and the effective mass, respectively. The thermoelectric calculations are performed with $n = 1 \times 10^{18}$ to $1 \times 10^{21} \text{ cm}^{-3}$ carrier concentrations at 50 to 800 K. To obtain the best thermoelectric efficiency of Ti_2O_3 under different pressures and carrier concentrations, we have compared the obtained results under various carrier concentration to each other. It is found that $n = 1 \times 10^{18} \text{ cm}^{-3}$ is an effective carrier concentration and it gives us the optimized achievement. Therefore, we have just presented the thermoelectric results with $n = 1 \times 10^{18} \text{ cm}^{-3}$. Here, the relaxation time is considered as a constant, and we have used the following relations²³:

$$\sigma_{\alpha\beta}(\varepsilon) = \frac{1}{N} \sum_{i,k} \sigma_{\alpha\beta}(i,k) \frac{\delta(\varepsilon - \varepsilon_{i,k})}{\delta(\varepsilon)}, \quad (3)$$

$$v_{\alpha\beta}(T; \mu) = \frac{1}{eT\Omega} \int \sigma_{\alpha\beta}(\varepsilon)(\varepsilon - \mu) \left\{ -\frac{\partial f_{\mu}(T; \varepsilon)}{\partial \varepsilon} \right\} d\varepsilon, \quad (4)$$

$$S_{ij} = (\sigma^{-1})_{\alpha i} v_{\alpha j}, \quad (5)$$

$$\kappa_{\alpha\beta}^0(T; \mu) = \frac{1}{e^2 T \Omega} \int \sigma_{\alpha\beta}(\varepsilon)(\varepsilon - \mu)^2 \left\{ -\frac{\partial f_{\mu}(T; \varepsilon)}{\partial \varepsilon} \right\} d\varepsilon, \quad (6)$$

where μ , f_{μ} and κ^0 are chemical potential, Fermi–Dirac distribution function and the electronic part of thermal conductivity ($\kappa^0 = \kappa_e$), respectively. The total thermal conductivity is composed of two electronic κ_e and lattice κ_l thermal conductivities ($\kappa = \kappa_e + \kappa_l$). A direct method for study of lattice thermal conductivity κ_l , is molecular dynamic simulation. A long simulation time need to calculate the κ_l and prediction of κ_l for Ti_2O_3 with the large unit cell is very expensive and it is impossible by Wien2k and BoltzTrap codes. On the other hand, there is not

experimental evidence for κ_l of Tl_2O_3 and compared to the previously reported results for Tl_2O show that κ_l of Tl_2O is below 1 W/mK³⁹ and it has a negligible contribution from the total thermal conductivity κ . Nevertheless, here we have calculated the electronic part of thermal conductivity κ_e .

For a semiconductor with a narrow band gap, the dependence of the Seebeck coefficient (S) on the effective mass of carriers is calculated as follows:

$$S = \frac{8\pi^2 k_B^2}{3eh^2} (m_1^* m_2^* m_3^*)^{1/3} N_v^{2/3} T \left(\frac{\pi}{3n}\right)^{2/3}, \quad (7)$$

$$m_i^* = \frac{\int e^{-\frac{dE(k)}{k_B T}} m_b^*(k) d(k)}{\int e^{-dE(k)/k_B T} dk}, \quad (8)$$

$$m_b^* = \frac{\hbar^2}{\frac{\partial^2 E(k)}{\partial k^2}}, \quad (9)$$

where \hbar , N_v , m_i^* and m_b^* are the Planck constant, band degeneracy, the mass components along three perpendicular directions ($i = x, y, z$) and band mass, respectively⁴⁰.

For study of optical spectra, the complex dielectric function is calculated. Dielectric function is the linear response of a system to electromagnetic waves and can be described by both the real $\varepsilon_1(\omega)$ and imaginary $\varepsilon_2(\omega)$ parts which are calculated as following relations⁴¹:

$$\varepsilon^{\alpha\beta}(\omega) = \varepsilon_1^{\alpha\beta}(\omega) + i\varepsilon_2^{\alpha\beta}(\omega), \quad (10)$$

$$\varepsilon_2^{\alpha\beta}(\omega) = \frac{\hbar^2 e^2}{\pi m^2 \omega^2} \sum_{c,v} \int dk \langle c_k | p^\alpha | v_k \rangle \langle v_k | p^\beta | c_k \rangle \delta(\varepsilon_{ck} - \varepsilon_{vk} - \omega), \quad (11)$$

$$\varepsilon_1^{\alpha\beta}(\omega) = \delta_{\alpha\beta} + \frac{2}{\pi} P \int_0^\infty \frac{\omega' \text{Im} \varepsilon_{\alpha\beta}(\omega')}{\omega'^2 - \omega^2} d\omega', \quad (12)$$

$$\alpha_{\alpha\alpha}(\omega) = \frac{\sqrt{2}\omega}{c} \sqrt{|\varepsilon_{\alpha\alpha}| - \text{Re}\varepsilon_{\alpha\alpha}(\omega)}, \quad (13)$$

$$E_{\text{loss}\alpha\alpha}(\omega) = \text{Im} \left(\frac{-1}{\varepsilon_{\alpha\alpha}(\omega)} \right). \quad (14)$$

Results and discussions

Optoelectronic results

The electronic band structure (B. S) of Tl_2O_3 was calculated using the mBJ and mBJ + SO potentials and the obtained B. S spectrum at zero pressure is shown in Fig. 1 by mBJ. A direct band gap E_g^F of 0.49 eV is appeared between top of the valence band Γ_2 and bottom of the conduction band Γ_3 . The experimental results show that there is a Bursntein-Moss shift $E_g^{B.M}$ about 0.74 eV in Tl_2O_3 compound between Γ_3 and Γ_4 points¹³. Therefore, widening of the band gap is about 1.23 eV. On the other hand, the optical band gap value at zero pressure was obtained by optical absorption calculations and compared with the electronic band structure. The results of the electrical and optical calculations for pure Tl_2O_3 and other TCOs have been summarized in Table 1. Obtained band gap value is in close agreement with the experiment. The bottom of the conduction band exhibit Tl-6s dangle band around the Γ point. The presence of parabolic curve, like free electrons in s state, justify the conductor behavior of Tl_2O_3 .

The calculated band structure of the Tl_2O_3 under pressure is plotted in Fig. 2. The band gap's nature is direct at Γ direction under all pressures. Obtained band gap values at zero pressure are achieved 0.49 and 0.45 eV for mBJ and mBJ + SO, respectively, which are in close agreement with the band gaps reported by other (see Table 1)^{8,9,35–39,42–46}. The variation of band gap values with pressures is shown in Fig. 3. It is observed that the band gap value linearly increases with pressure and band gap values by mBJ are more than mBJ + SO at all pressures. We have fitted two linear relations between band gap values and pressures as:

$$E_g^{\text{mBJ}} = 0.01891 P + 0.5114; E_g^{\text{mBJ+SO}} = 0.01869 P + 0.4665. \quad (15)$$

The results indicate that it is possible to control the band gap value and the other optoelectronic and thermoelectric properties by pressure. Nevertheless, we to predict the transport properties of electrons under applied pressure by the calculation of the effective mass of carries from the curvature of band structure plots. To clarify the effective mass of electrons under pressure, the curvature of electronic bands in the bottom of the conduction band are investigated at $\Gamma \rightarrow P$ direction by Eq. (9). As shown in Fig. 4, with increasing pressure, the effective mass of electrons is increased and the electron mobility decreases. It should be noted that by increasing pressure,

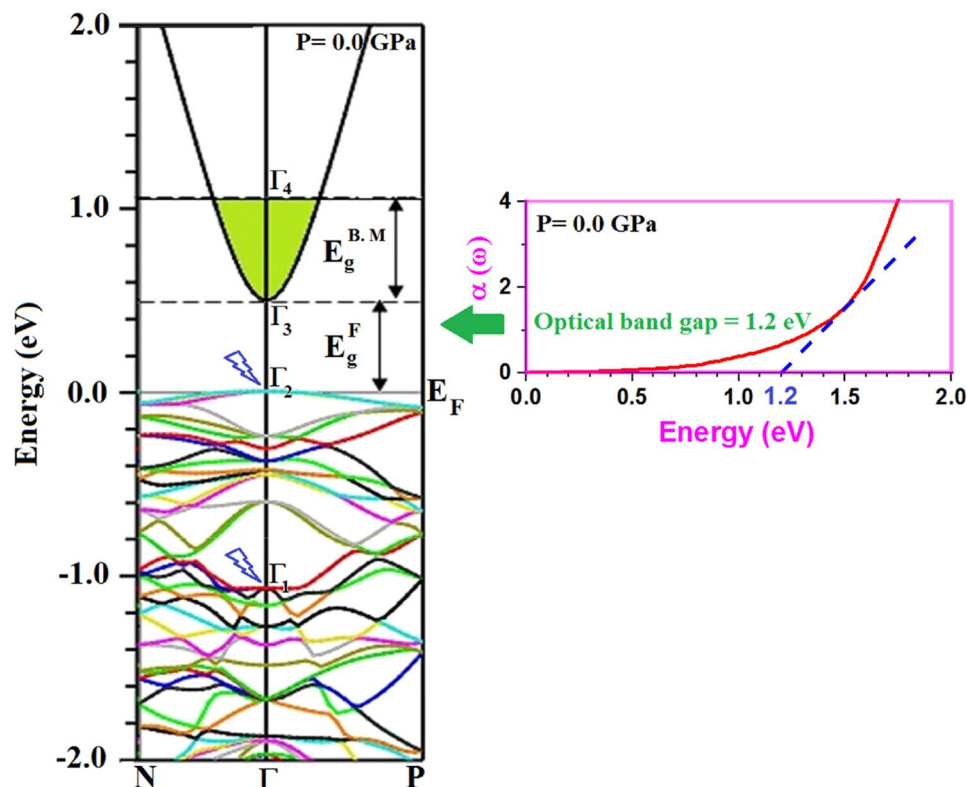


Figure 1. Calculated band structure of Tl_2O_3 and band gap engineering by $m\text{BJ}$ at zero pressure. Obtained band gap is compared with the calculated absorption spectra at zero pressure.

TCOs	E_g^{DFT} (eV)	E_g^{Exp} (eV)	$\epsilon(0)$	ZT	S ($\mu\text{V}/\text{K}$)
Tl_2O_3	1.23, 1.1 ^a	1.4 ^b , 1.6 ^c	4.80	0.82(n-type), 0.98 (p-type)	- 292 (n-type), 775 (p-type)
In_2O_3	0.99 ^d , 1.2 ^e	2.61 ^d	4.73(DFT) ^d , 4.0 (Exp.) ^d	-	320 ^f
Tl_2O	0.93 ^g , 1.62 ^h	-	-	0.96 ^h , 0.94 ^h	-
HgO	1.17 ^g , 1.28 ⁱ	2.2 ^c , 1.9 ^c	-	0.58 ⁱ	-
$\text{In}_{1.5}\text{Co}_{0.5}\text{O}_3$	1.3 ^f , 0.8 ^f	-	4.41 ^f	-	-
$\text{In}_{1.5}\text{La}_{0.5}\text{O}_3$	3.03 ^j	4.03 ^j	3.12 ^j	-	-
SnO_2	1.76 ^k	3.41 ^k , 3.87 ^l	-	-	255 ^l
$\alpha\text{-Ga}_2\text{O}_3$	2.86 ^k	4.9 ^k	-	-	-
$\beta\text{-Ga}_2\text{O}_3$	2.29 ^k	4.61 ^k	4.37 ^m	-	290(Exp.) ^f , 341 (DFT) ^f

Table 1. Obtained optoelectronic and thermoelectric properties (at 300 K) of Tl_2O_3 and compared with the other TCO materials. ^aRef.⁷, ^bRef.⁸, ^cRef.⁹, ^dRef.³⁸, ^eRef.³⁶, ^fRef.⁴¹, ^gRef.³⁹, ^hRef.⁴², ⁱRef.⁴³, ^jRef.³⁵, ^kRef.⁴⁴, ^lRef.⁴⁵, ^mRef.⁴⁶.

the lattice constants and hence bond lengths decrease and the interaction between electrons and ions increases which results in the change the effective mass of electrons.

The calculated total and partial densities of states (DOSs) of Tl_2O_3 are presented in Fig. 5a at zero pressure. Three main regions are observed in DOS spectra. The first region is observed in -19 to -16 eV. It is a mixture of the O-2 s states with a few contributions of Tl-6 s, 4f, and 6p states. The second region is created in the -10 to 0 eV near the Fermi level. It is considerably dominated by Tl-5d, 6 s, 6p, and 4f states and O-2p states while in the third region at the bottom of the conduction band, Tl-6 s and O-2p states play a key role in electronic behavior of Tl_2O_3 .

Pressure dependence of the DOSs are plotted in Fig. 5b. It is clear that by increasing pressure, the valence band maximum is nearly constant while the conduction band minimum is shifted upward. It is found that the effect of hydrostatic pressure significantly shifts the Tl-6s state in the bottom of the conduction band. Electronic results show that pressure tuning is an effective way to control the physical properties of TCOs.

In Fig. 6a and b, the real and imaginary parts of the dielectric function are plotted at different pressures. Obtained static dielectric constants at zero photon energy, $\epsilon_1(0)$, are 4.8, 4.62, 4.4, 4.3, and 4.2 at 0.0, 4.9, 10.5, 15.0 and 22.0 GPa, respectively which compared with similar TCOs in Table 1^{31,32,34}. It is also found that $\epsilon_1(0)$

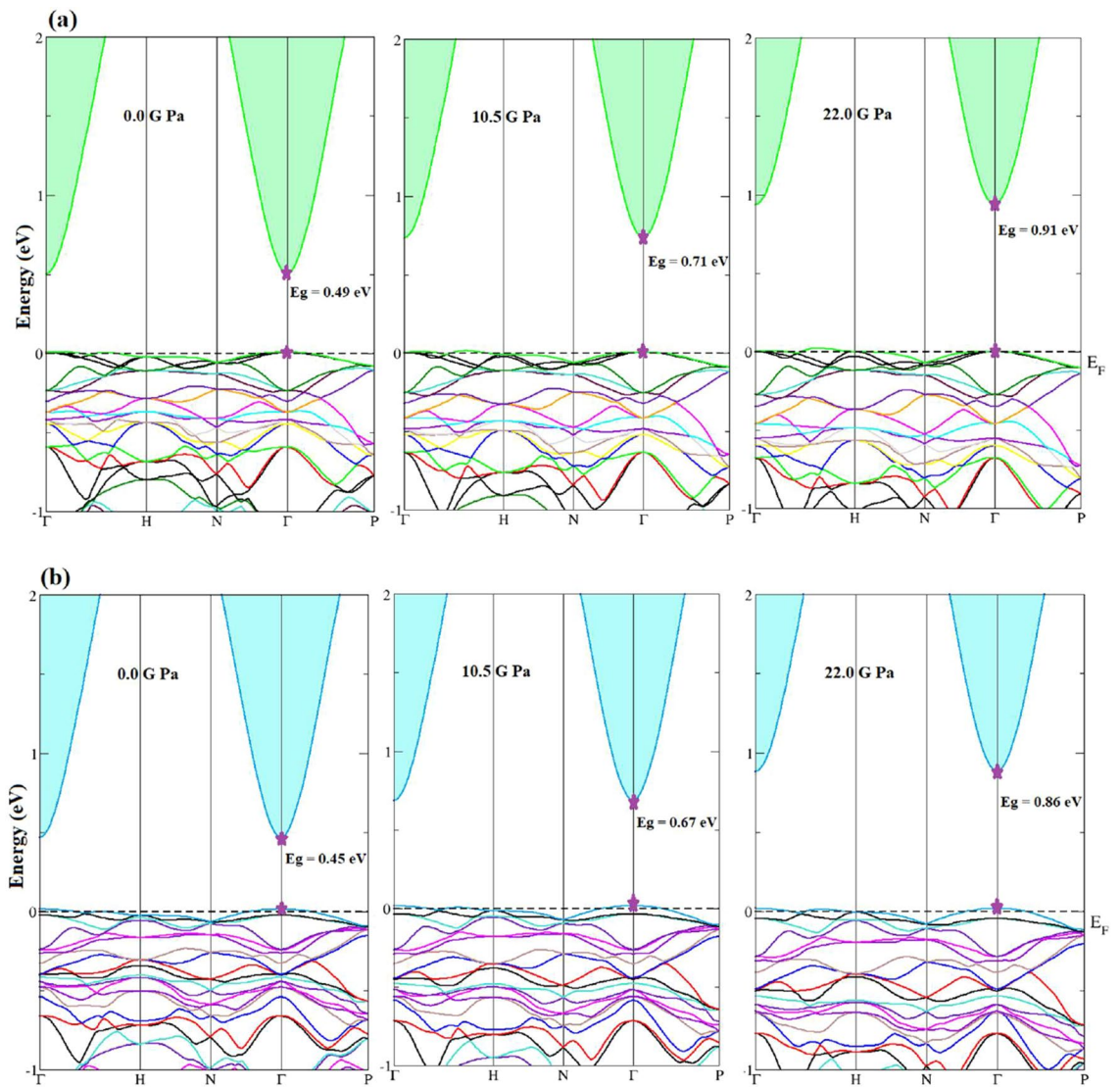


Figure 2. Calculated band structures of Tl_2O_3 under pressure by (a) *mBJ* and (b) *mBJ+SO*.

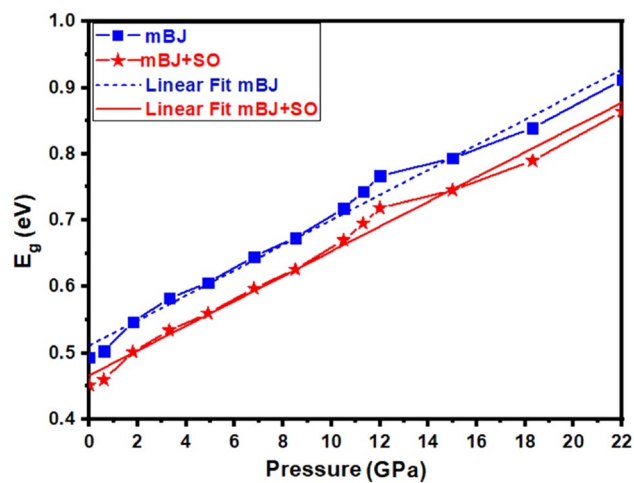


Figure 3. The variation of the band gap value with respect to the pressure for Tl_2O_3 .

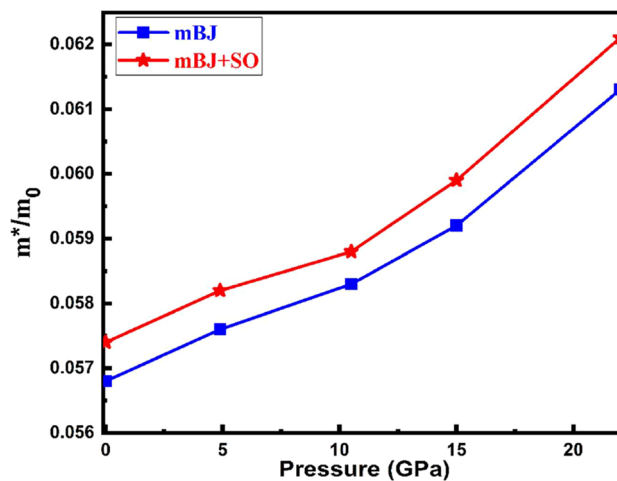


Figure 4. The variation of the effective mass of electrons with respect to the pressure for Tl_2O_3 .

decreases with increasing pressure. Tl_2O_3 can be used in semiconductor devices because of the inverse relationship between the static dielectric constants and semiconductor band gap which verifies by the Penn model⁴⁷ ($\epsilon_1(0) \approx 1 + (\frac{\hbar\omega_p}{E_g})^2$).

By increasing pressure, the main peaks, corresponding to the different pressures, are shifted towards higher energies. For the first and second main peaks, the intensity of peaks decreases with an increase in pressure while for the other main peaks near to the zero value $\epsilon_1(\omega)$ the intensity of peaks increases with pressure. After some fluctuations, it reaches to zero value at 0.0 GPa in the range of 21.0 and 24.0 eV. It is clear that the negative value of $\epsilon_1(\omega)$ is almost appeared with increasing pressure. In this region, the material exhibits a high reflection with metallic nature. After 25 eV, we can see the positive value of $\epsilon_1(\omega)$ and the overall trend of $\epsilon_1(\omega)$ remains the same at the high energy of incident photons under the effect of pressure.

As shown in Fig. 6b, the main peaks of the imaginary part of the dielectric function, $\epsilon_2(\omega)$, are corresponding to the optical transitions of electrons from the valence band to the conduction band around the E_p . The optical band gap or threshold energy of $\epsilon_2(\omega)$ spectrum is shown as E_i , correspond to direct inter-band transitions from $\Gamma_2 \rightarrow \Gamma_4$ in Fig. 1. By increasing pressure, this value increase. The second strong peak E_2 is corresponding to the optical transitions $\Gamma_1 \rightarrow \Gamma_4$, as it is observed in the experimental absorption measurements⁹. Other main peaks are related to the electronic transitions from the deep electronic states in the valence band to the conduction band³⁵.

The electron energy loss spectrum, EELS, is a useful optical spectrum for prediction of Plasmon energies. The electron density in the material plays a key role in the excitation of the plasmons. Figure 6c shows the calculated EELS spectra. EELS is zero at low energies below the optical band gap without scattering of electrons. By enhancing the energy of incident photons, EELS increases slowly due to the inelastic scattering of electrons. EELS spectrum reaches to the maximum value then decreases. The maximum energy value of EELS corresponds to the Plasmon energy. Obtained Plasmon energies are 24, 24.2, 24.55, 24.69 and 25.38 eV at 0.0, 4.9, 10.5, 15.0 and 22 GPa, respectively. It is clear that the Plasmon energy is shifted to the higher value of EELS with increasing pressure.

In Fig. 6d, the pressure- dependent of absorption spectra of Tl_2O_3 are displayed at the energy range of 0–35 eV. By increasing pressure, the absorption value increase from 146.72 to $163.47 \times 10^4 \text{ cm}^{-1}$ and a blue shift is observed towards higher values in the energy of incident photons correspond to the energy range of 15.32–20.54 eV in the ultraviolet UV spectrum. As shown in the inset of Fig. 6d, there is not absorption for photons with energies lower than optical band gap and absorption start with an increase in photon energy. It is clear that optical band gap increase with an increase in pressure.

Thermoelectric results

As shown in Fig. 7, the Seebeck coefficient (SC) of Tl_2O_3 is calculated as a function of carrier concentration, pressure, and temperatures for both *n*- and *p*-types Tl_2O_3 . The Seebeck coefficient is negative for *n*-type Tl_2O_3 and it is positive for *p*-type. It is observed that the SC increase with increasing temperature then it decreases with temperature as defined in Eq. (7). The SC is directly proportional to the temperature and it is inversely proportional to the carrier concentration. Therefore, the SC increase with temperature at low temperature. On the other hand, at high temperatures, the carrier concentration *n* is thermally excited hence by increasing *n*, the SC decreases. Obtained SC, at room temperature (300 K) for *n*- type Tl_2O_3 , are –268, –275, –281, –286 and –292 $\mu\text{V}/\text{K}$ at 0.0, 4.9, 10.5, 15.0 and 22 GPa, respectively. The results show that with increasing pressure, the SC for *n*-type one increases and it is almost similar for *p*-type one in the temperature range of 50–350 K.

As shown in Fig. 4 and defined in Eq. (7), by increasing pressure, the effective mass of electrons increases which results an increased SC of *n*- type Tl_2O_3 . For *p*- type Tl_2O_3 with increase in pressure, the hole states in the valence band are nearly constant (Fig. 2) and hence its changes with pressure is almost small. It is also seen that the more effect of pressure on SC is at high temperatures.

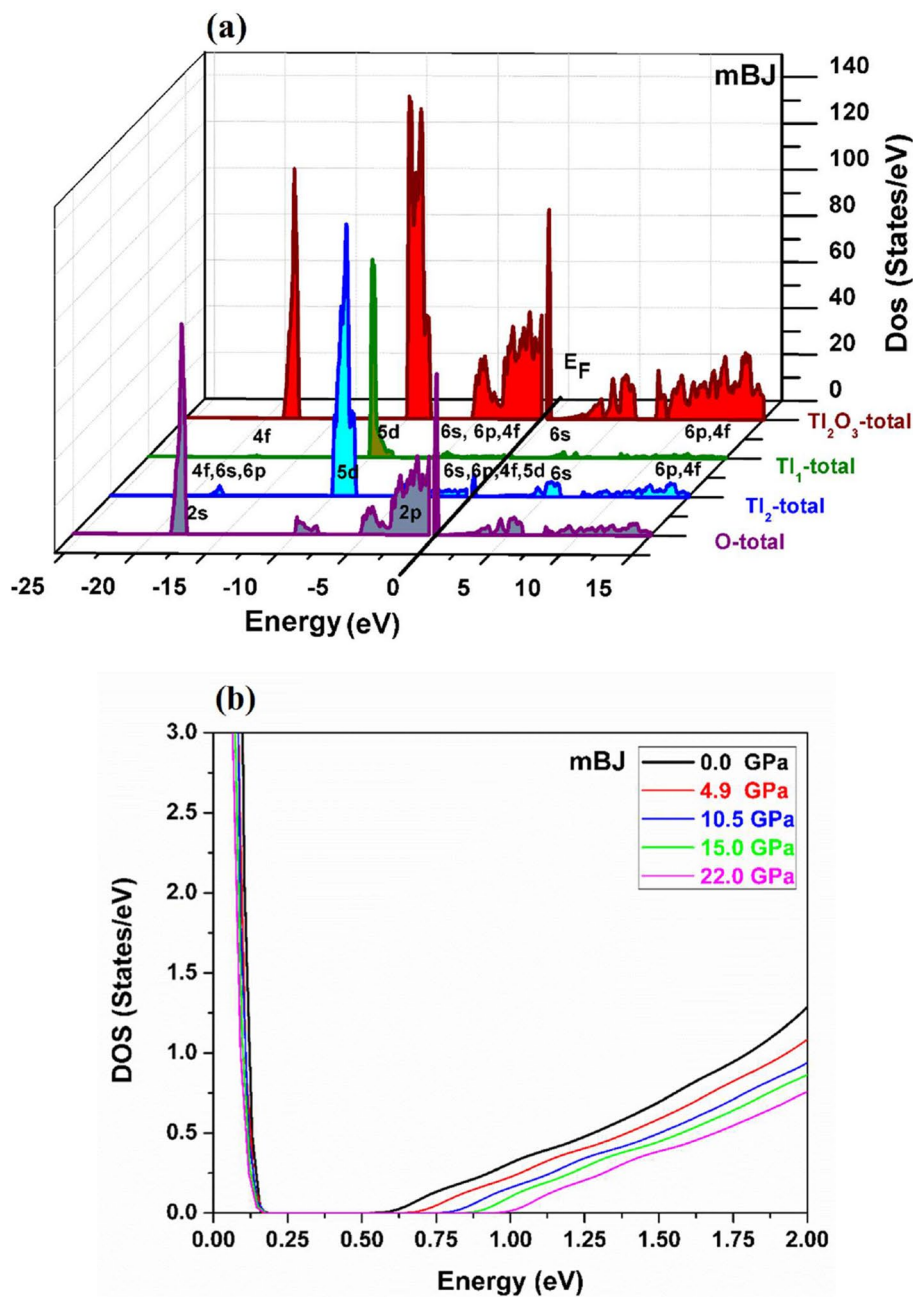


Figure 5. Density of states of Tl_2O_3 (a) at zero pressure and (b) different pressures by *mBJ*.

The calculated electrical conductivity (σ/τ) is plotted in Fig. 8. In this plot, the variation of σ/τ with $n = 1 \times 10^{18} \text{ cm}^{-3}$ carrier concentration, temperature and pressure are studied. The electrical conductivity is almost constant at low temperature 450 K then it increases by increasing temperature and excitation of carrier concentration as following relation:

$$\sigma = ne\mu, \quad (16)$$

where μ is the mobility. The figure shows that the electrical conductivity (σ/τ) remains almost constant with enhancing temperature at high pressure (22.0 GPa).

The pressure and temperature dependences of electronic part of thermal conductivity (κ_e/τ) are displayed in Fig. 9 for n- and p- type Tl_2O_3 at $n = 1 \times 10^{18} \text{ cm}^{-3}$ carrier concentration. Electronic thermal conductivity depends upon carrier concentration and temperature, as follows:

$$k_e = \frac{n\pi^2 T k_b^2}{3m^* v_e}. \quad (17)$$

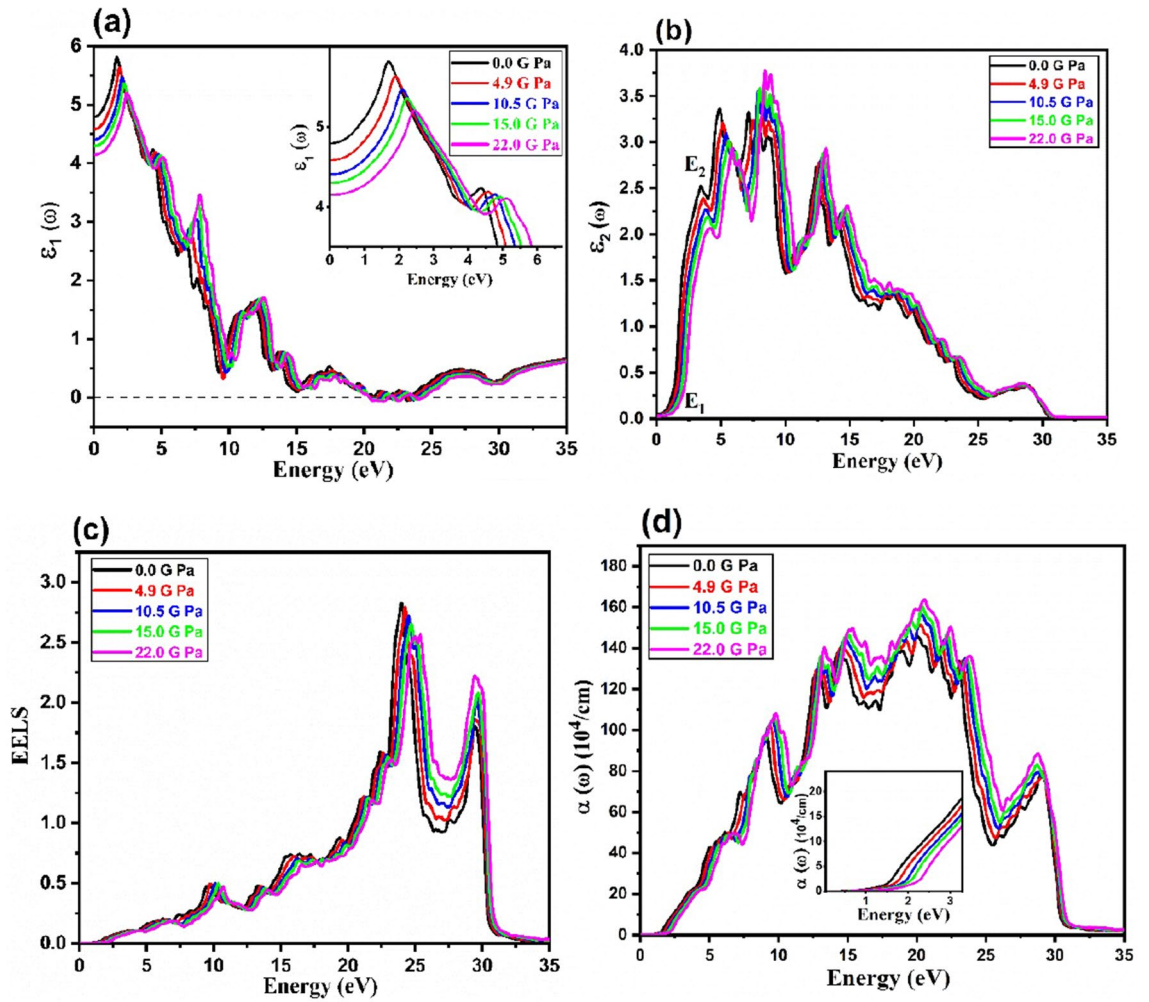


Figure 6. Calculated optical spectra for Ti_2O_3 at various pressures (a) the real part of dielectric function, (b) the imaginary part of dielectric function (c) the electron energy loss spectrum EELS and (d) Absorption.

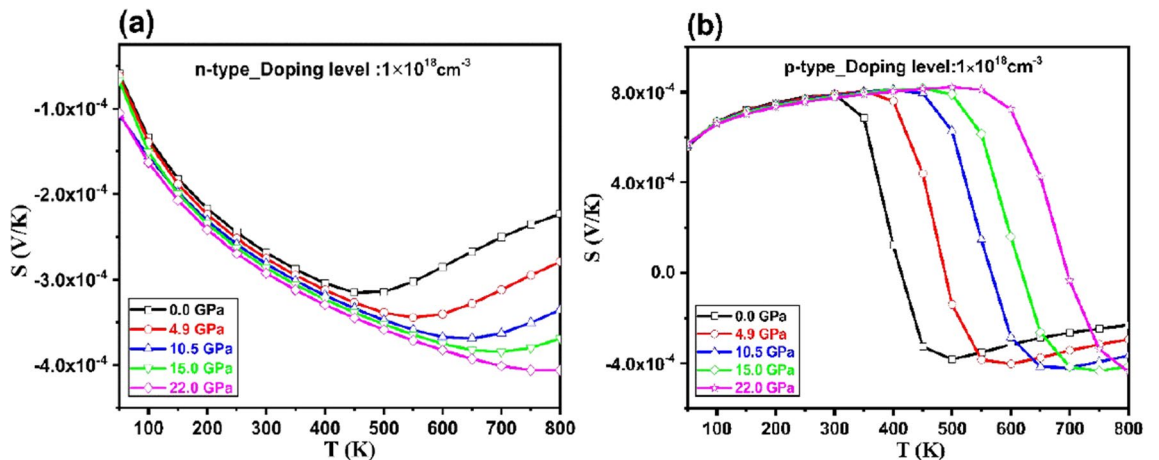


Figure 7. The variation of Seebeck coefficient with respect to the temperature and pressure at $n = 1 \times 10^{18} \text{ cm}^{-3}$ carrier concentration for (a) n - and (b) p -types of Ti_2O_3 .

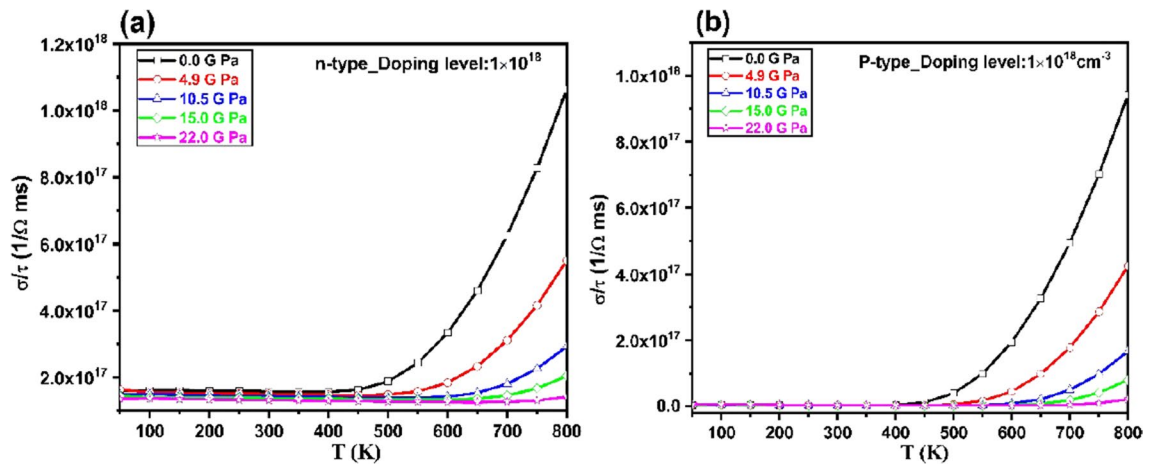


Figure 8. The variation of electrical conductivity with respect to the temperature and pressure at $n = 1 \times 10^{18} \text{ cm}^{-3}$ carrier concentration for (a) n - and (b) p -types Tl_2O_3 .

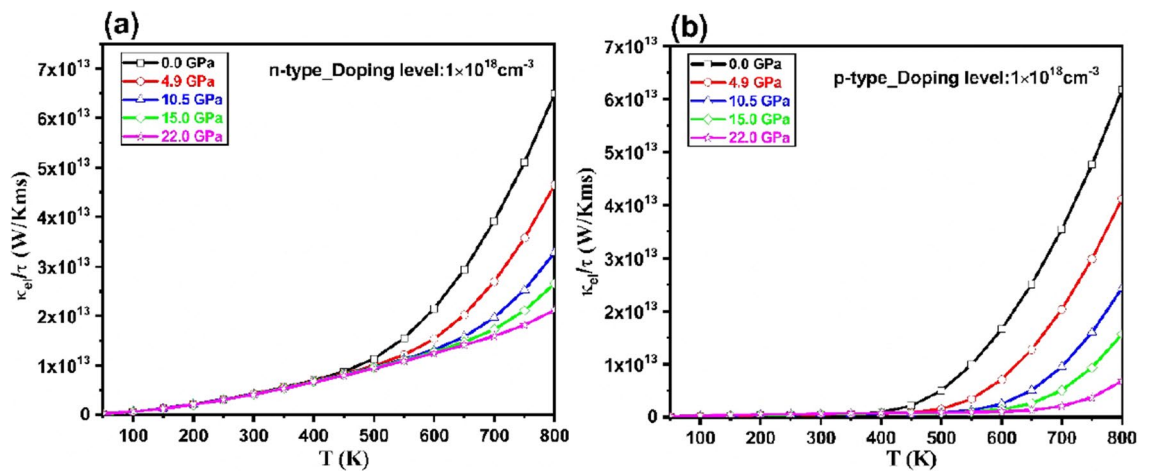


Figure 9. The variation of thermal conductivity with respect to the temperature and pressure at $n = 1 \times 10^{18} \text{ cm}^{-3}$ carrier concentration for (a) n - and (b) p -types of Tl_2O_3 .

It is clear that by the increase in temperature, the electrical conductivity increases and it remains constant at all pressures at low temperatures. An increasing trend is observed just in n -type Tl_2O_3 which correspond the electronic states in the conduction band, with the pressure effect at low temperatures. At high temperatures, with the increase in pressure, the effective mass of carries increase, so the electronic thermal conductivity decreases. The maximum value of κ_e/τ for n -type Tl_2O_3 is obtained about $6.5 \times 10^{13} \text{ W}/\text{Kms}$ at 800 K and zero pressure.

In Fig. 10, the variation of figure of merit (ZT) are shown with temperature and pressure at $n = 1 \times 10^{18}$ carrier concentration. ZT increases with increasing in temperature and pressure. At room temperature, the ZT values of 0.82 and 0.98 K achieved at 22.0 GPa, for n and p -types Tl_2O_3 , respectively. High pressure as well as temperature have a strong effect on the figure of merit (ZT) of Tl_2O_3 . In Table 1, obtained results are compared with the thermoelectric properties of TCOs. These thermoelectric findings imply that this TCO material can be used in the fabrication of thermoelectric devices under pressure.

Conclusion

The effect of pressure on the structural, optoelectronic and thermoelectric properties of Tl_2O_3 were investigated by using the FP-LAPW method and the modified Becke-Johnson (mBJ) functional with spin-orbit coupling. In band structure, obtained direct band gap of Tl_2O_3 is 1.23 eV at zero pressure. The results show that the band gap and the effective mass of carries increases with pressure. The bottom of the conduction band composed of Tl-6s dangle band and the hydrostatic pressure significantly shifts Tl-6s state. By increasing pressure, the blue shift observed in optical responses such as the real and the imaginary parts of the dielectric functions, electron energy loss and absorption spectra. For n -type Tl_2O_3 , the Seebeck coefficient increases with pressure and reaches to $-292 \mu\text{V}/\text{K}$ at room temperature but thermal conductivity decrease under the effect of pressure. By increasing pressure, it is possible to control the high Seebeck coefficient and the low thermal conductivity for

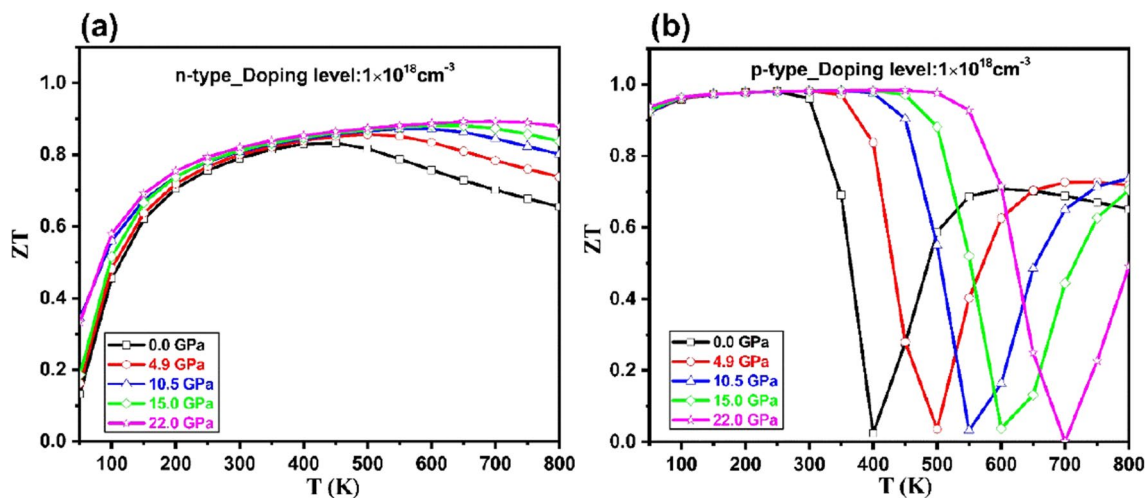


Figure 10. The variation of figure of merit (ZT) with respect to the temperature and pressure at $n = 1 \times 10^{18} \text{ cm}^{-3}$ carrier concentration for (a) n - and (b) p -types of Tl_2O_3 .

Tl_2O_3 compound. The maximum figure of merit ZT of p -type Tl_2O_3 is 0.98. The results indicate that pressure and temperature tuning play significant roles in the design of thermoelectric devices based on Tl_2O_3 .

Data availability

The data that support the findings of this study are available from the corresponding author H. A. Rahnamaye Aliabad, upon reasonable request.

Received: 10 January 2024; Accepted: 2 April 2024

Published online: 22 April 2024

References

- Walia, S. *et al.* Transition metal oxides-thermoelectric properties. *Prog. Mater. Sci.* **58**, 1443–1489 (2013).
- Hosseini, S. M., Rahnamaye Aliabad, H. A. & Kompany, A. Electronic and thermoelectric properties of pure and alloys In_2O_3 transparent conductors. *Mod. Phys. Lett. B* **24**, 2251–2265 (2010).
- Zhu, Q., Hopper, E. M., Ingram, B. J. & Mason, T. O. Combined Jonker and Ioffe analysis of oxide conductors and semiconductors. *Am. Ceram. Soc.* **94**, 187–193 (2011).
- Ren, G. *et al.* High performance oxides-based thermoelectric materials. *JOM* **67**, 211–221 (2015).
- Ha, V.-A. *et al.* Computationally driven high-throughput identification of CaTe and Li_3Sb as promising candidates for high-mobility p -type transparent conducting materials. *Phys. Rev. Mater.* **3**(3), 034601 (2019).
- Phillips, R. J., Shane, M. J. & Switzer, J. A. Electrochemical and photoelectrochemical deposition of thallium (III) oxide thin films. *Mater. Res.* **4**, 923–929 (1989).
- Kehoe, A. B., Scanlon, D. O. & Watson, G. W. Nature of the band gap of Tl_2O_3 . *Phys. Rev. B* **83**, 233202 (2011).
- Geserich, H. P. Optical and electrical measurements on thallium III oxide thin films. *Phys. Status Solidi* **25**, 741–751 (1968).
- Glans, P. A. *et al.* Experimental and theoretical study of the electronic structure of HgO and Tl_2O_3 . *Phys. Rev. B* **71**, 235109 (2005).
- Goto, A., Yasuoka, H., Hayashi, A. & Ueda, Y. NMR study of metallic thallic oxides; $\text{Tl}_2\text{O}_3 - \delta$. *J. Phys. Soc. Jpn.* **61**, 1178–1181 (1992).
- Shukla, V. N. & Wirtz, G. P. Electrical conduction in single-crystal thallic oxide: I, crystals “as-grown” from the vapor in air. *Am. Ceram. Soc.* **60**, 253–258 (1977).
- Shukla, V. N. & Wirtz, G. P. Electrical conduction in single-crystal thallic oxide: II, effects of annealing at 923° K in oxygen pressures from 0.01 to 1 atmosphere. *Am. Ceram. Soc.* **60**, 259–261 (1977).
- Wirtz, G. P., Yu, C. J. & Doser, R. W. Defect chemistry and electrical properties of thallium oxide single crystals. *Am. Ceram. Soc.* **64**, 269–275 (1981).
- Van Leeuwen, R. A., Hung, C. J., Kammler, D. R. & Switzer, J. A. Optical and electronic transport properties of electrodeposited thallium (III) oxide films. *Phys. Chem.* **99**, 15247–15252 (1995).
- Scanlon, D. O. *et al.* Band gap engineering of In_2O_3 by alloying with Tl_2O_3 . *Appl. Phys. Lett.* <https://doi.org/10.1063/1.4860986> (2013).
- Jackson, A. J. *et al.* Computational prediction and experimental realization of Earth-Abundant transparent conducting oxide Ga-Doped ZnSb_2O_6 . *ACS Energy Lett.* **7**(11), 3807–3816 (2022).
- Zhang, J. J. *et al.* Deep UV transparent conductive oxide thin films realized through degenerately doped wide-bandgap gallium oxide. *Cell Rep. Phys. Sci.* **3**(3), 100801 (2022).
- Burstein, E. Anomalous optical absorption limit in InSb . *Phys. Rev.* **93**(3), 632 (1954).
- Patra, C. R. & Gedanken, A. Rapid synthesis of nanoparticles of hexagonal type In_2O_3 and spherical type Tl_2O_3 by microwave irradiation. *N. J. Chem.* **28**(8), 1060–1065 (2004).
- Rahnamaye Aliabad, H. A., Basirat, S. & Ahmad, I. Structural, electrical and thermoelectric properties of CdGa_2S_4 compound under high pressures by mBJ approach. *Mater. Sci. Mater. Electron.* **28**, 16476 (2017).
- Abareishi, A. & Rahnamaye Aliabad, H. A. Anisotropic thermoelectric properties of $\text{Sr}_5\text{Sn}_2\text{As}_6$ compound under pressure by PBE-GGA and mBJ approaches. *Mater. Res. Express* **4**, 096303 (2017).
- Rahnamaye Aliabad, H. A., Nodehi, Z., Maleki, B. & Abareishi, A. Electrical and thermoelectric properties of half-Heusler ZrNiPb under pressure in bulk and nanosheet structures for energy conversion. *Rare Met.* **38**, 1015–1023 (2019).

23. Rahnamaye Aliabad, H. A. & Asadi Rad, F. Structural, electronic and thermoelectric properties of bulk and monolayer of Sb_2Se_3 under high pressure: By GGA and mBJ approaches. *Phys. B Condens. Matter* **545**, 275–284 (2018).
24. Rahnamaye Aliabad, H. A. & Hosseini, N. Effect of substituted Ca on the thermoelectric and optoelectronic properties of NaRh_2O_4 under pressure. *Electron. Mater.* **47**, 2009–2016 (2018).
25. Rahnamaye Aliabad, H. A. & Yalcin, B. G. Optoelectronic and thermoelectric response of $\text{Ca}_5\text{Al}_2\text{Sb}_6$ to shift of band gap from direct to indirect. *Mater. Sci. Mater. Electron.* **28**, 14954–1964 (2017).
26. Matsumoto, R. *et al.* Pressure-induced insulator to metal transition of mixed valence compound $\text{Ce}(\text{O}, \text{F})\text{SbS}_2$. *Appl. Phys.* **125**, 075102 (2019).
27. Guo, H., Yang, T., Tao, P., Wang, Y. & Zhang, Z. High pressure effect on structure, electronic structure, and thermoelectric properties of MoS_2 . *Appl. Phys.* **113**, 013709 (2013).
28. Su, T. *et al.* Thermoelectric properties of $\text{PbTe}_{1-x}\text{Se}_x$ alloys prepared by high pressure. *Phys. Chem. Solids* **74**, 913–916 (2013).
29. Rahnamaye Aliabad, H. A., Rabbanifar, S. & Khalid, M. Structural, optoelectronic and thermoelectric properties of FeSb_2 under pressure: Bulk and monolayer. *Phys. B Condens. Matter* **570**, 100–109 (2019).
30. Mohammadkhani, A., Bagheri, G. H. A. & Rayati, S. X-shaped thallium oxide nanostructures as a high performance photocatalyst for degradation of Cephalexin. *Part. Sci. Technol.* **15**(2), 117–122 (2019).
31. Gomis, O. *et al.* High-pressure structural and elastic properties of Ti_2O_3 . *Appl. Phys.* **116**, 133521 (2014).
32. Schwarz, K., Blaha, P. & Madsen, G. K. H. Electronic structure calculations of solids using the WIEN2k package for material sciences. *Comput. Phys. Commun.* **147**, 71–76 (2002).
33. Georg, K., Madsen, H. & Singh, D. J. BoltzTraP. A code for calculating band-structure dependent quantities. *Comput. Phys. Commun.* **175**(67), 71 (2006).
34. Tran, F. & Blaha, P. Accurate band gaps of semiconductors and insulators with a semilocal exchange-correlation potential. *Phys. Rev. Lett.* **102**, 226401 (2009).
35. Rahnamaye Aliabad, H. A. Theoretical and experimental studies of La- substituted In_2O_3 nano-layer via the modified Becke-Johnson (mBJ) potential. *Optik* **175**, 268–274 (2018).
36. Rahnamaye Aliabad, H. A. *et al.* Optoelectronic properties of pure and co-doped indium oxide by Hubbard and modified Becke-Johnson exchange potentials. *Chin. Phys. Lett.* **30**, 127101 (2013).
37. Rahnamaye Aliabad, H. A. Investigation of optoelectronic properties of pure and Co substituted $\alpha\text{-Al}_2\text{O}_3$ by Hubbard and modified Becke-Johnson exchange potentials. *Chin. Phys. B* **24**, 097102 (2015).
38. Rahnamaye Aliabad, H. A., Asadi, Y. & Ahmad, I. Quasiparticle optoelectronic properties of pure and doped indium oxide. *Opt. Mater.* **34**, 1406–1414 (2012).
39. Li, J. H., Wu, J. & Yu, Y. X. Theoretical exploration of single-layer Ti_2O as a catalyst in lithium–oxygen battery cathodes. *Phys. Chem. C* **124**, 9089–9098 (2020).
40. Zevalkink, A. *et al.* Influence of the Tritel elements ($M = \text{Al}, \text{Ga}, \text{In}$) on the transport properties of $\text{Ca}_5\text{M}_2\text{Sb}_6$ zintl compounds. *Chem. Mater.* **24**, 2091–2098 (2012).
41. Kumar, A. & Singiseti, U. First-principles study of thermoelectric properties of β -gallium oxide. *Appl. Phys. Lett.* <https://doi.org/10.1063/5.0027791> (2020).
42. Sajjad, M., Singh, N., Sattar, S., De Wolf, S. & Schwingenschlöggl, U. Ultralow lattice thermal conductivity and thermoelectric properties of monolayer Ti_2O . *ACS Appl. Energy Mater.* **2**, 3004–3008 (2019).
43. Liu, J., Zhao, Y., Dai, Z., Ni, J. & Meng, S. Low thermal conductivity and good thermoelectric performance in mercury chalcogenides. *Comput. Mater. Sci.* **185**, 109960 (2020).
44. Y. Song, Novel transparent conductive materials: understanding and prediction. https://scholarsmine.mst.edu/masters_theses/5428 (2011)
45. Bagheri-Mohagheghi, M. M., Shahtahmasebi, N., Alinejad, M. R., Youssefi, A. & Shokooh-Saremi, M. Fe-doped SnO_2 transparent semi-conducting thin films deposited by spray pyrolysis technique: Thermoelectric and p-type conductivity properties. *Solid State Sci.* **11**, 233–239 (2009).
46. Liu, Q., Chen, Z. & Zhou, X. Electronic, thermal, and thermoelectric transport properties of $\epsilon\text{-Ga}_2\text{O}_3$ from first principles. *ACS Omega* **7**, 11643–11653 (2022).
47. Penn, D. R. Wave-number-dependent dielectric function of semiconductors. *Phys. Rev.* **128**(5), 2093 (1962).

Acknowledgements

We thank Prof. Blaha and Prof. Madsen of Vienna University of Technology, Austria for their help in the use of Wien2k and BoltzTrap packages.

Author contributions

H. A. Rahnamaye Aliabad was responsible for manuscript preparation, performing calculations, and conceptualization. A. Asadpour Arzefooni and Seyede Zeinab Sadati provided editing assistance, formal analysis and figure generation. P. Khosrojerdi contributed to formal analysis. Evren Görkem Özdemir was involved in formal analysis. All authors reviewed the manuscript.

Competing interests

The authors declare no competing interests.

Additional information

Correspondence and requests for materials should be addressed to H.A.R.A.

Reprints and permissions information is available at www.nature.com/reprints.

Publisher's note Springer Nature remains neutral with regard to jurisdictional claims in published maps and institutional affiliations.



Open Access This article is licensed under a Creative Commons Attribution 4.0 International License, which permits use, sharing, adaptation, distribution and reproduction in any medium or format, as long as you give appropriate credit to the original author(s) and the source, provide a link to the Creative Commons licence, and indicate if changes were made. The images or other third party material in this article are included in the article's Creative Commons licence, unless indicated otherwise in a credit line to the material. If material is not included in the article's Creative Commons licence and your intended use is not permitted by statutory regulation or exceeds the permitted use, you will need to obtain permission directly from the copyright holder. To view a copy of this licence, visit <http://creativecommons.org/licenses/by/4.0/>.

© The Author(s) 2024